PCCP

RSC Publishing

PAPER

View Article Online
View Journal | View Issue

Cite this: *Phys. Chem. Chem. Phys.*, 2013, **15**, 8672

A variable temperature synchrotron X-ray diffraction study of the ferroelastic double perovskite Ba_2GdMoO_6

Thomas K. Wallace, Ross H. Colman and Abbie C. Mclaughlin*

Received 23rd October 2012,
Accepted 30th December 2012

DOI: 10.1039/c2cp43732e

www.rsc.org/pccp

A study of the magnetic and structural properties of the double perovskite Ba_2GdMoO_6 has been performed. The crystal structure distorts from the ideal cubic ($Fm\bar{3}m$) structure to the tetragonal space group $I4/m$ at 220 K, before undergoing a second distortion to a triclinic system ($I\bar{1}$) at 80 K. The phase transition to triclinic symmetry is also evident in magnetic susceptibility measurements. The variable temperature synchrotron powder X-ray diffraction results reveal that Ba_2GdMoO_6 is ferroelastic, with the onset of ferroelastic domain formation occurring at the cubic–tetragonal phase transition. A number of Rietveld refinement techniques for modelling diffuse scattering from ferroelastic domain boundaries have been explored.

I. Introduction

Transition metal perovskites (ABX_3) have received much attention as a result of their diverse properties. These include colossal magnetoresistance (CMR) as observed in doped manganites such as $La_{1-x}Sr_xMnO_3$,[1] ferroelectricity in $BaTiO_3$,[2] superconductivity in $Ba_{1-x}K_xBiO_3$[3] and ferroelasticity in $LaCoO_3$.[4] As well as these useful properties, it is the ability to easily adapt the perovskite structure by chemical substitution and produce materials with optimised properties that makes studying the perovskites such an attractive proposition.

Double perovskites have the general formula $A_2BB'X_6$ and are formed by extension of the basic perovskite structure, where a mixture of cations occupy the octahedrally coordinated B sites.[5] Within this B site sub-lattice, cations can be disordered; or ordered in a layered, columnar or rock salt arrangement. As with the basic perovskite structure, double perovskites regularly undergo symmetry lowering distortions such as octahedral tilting,[5] B site cation displacements[6,7] and orbital ordering leading to Jahn–Teller (JT) distortions.[8] Such structural flexibility results in extremely versatile materials that readily undergo distortions away from the ideal cubic symmetry.

Double perovskites also exhibit diverse electronic and magnetic properties. Superconductivity has been evidenced in doped double perovskites such as $A_2Y(Ru_{1-x}Cu_x)O_6$ (where A = Ba or Sr),[9] $Sr_2MgMoO_{6-\delta}$ is an oxide ion conductor with potential application in solid oxide fuel cells,[10] low field magnetoresistance has been observed in Sr_2FeMoO_6[11] and ferroelasticity has been reported for materials such as Ba_2GdNbO_6.[12] More recently, there have been a number of studies of Mo^{5+} double perovskites with chemical formula Ba_2LnMoO_6[13–16] where Ln = lanthanide or Y^{3+} ion. Ba_2LnMoO_6 materials are electrically insulating and show antiferromagnetic interactions between Mo^{5+} $S = 1/2$ spins.[13–15] Across this series, a picture of the magnetic and structural behaviour of these materials is beginning to emerge. No evidence for magnetic order has been reported down to 2 K in Ba_2LnMoO_6 (RE = Gd, Dy–Yb and Y).[13,14] However, the substitution of rare earth cations with larger ionic radii induces antiferromagnetic ordering. This ordering is observed at the anomalously high temperatures of T_N = 112 K in Ba_2EuMoO_6 (r_{Eu} = 0.947 Å), T_N = 130 K in $Ba_2{}^{154}SmMoO_6$ (r_{Sm} = 0.958 Å) and at the lower temperature of T_N = 15 K, in Ba_2NdMoO_6 (r_{Nd} = 0.983 Å).[13,15,17]

Detailed variable temperature neutron diffraction studies on $Ba_2{}^{154}SmMoO_6$ and Ba_2NdMoO_6 have revealed further differences between the two materials.[15,18] In both materials, distortions from a higher symmetry tetragonal (space-group $I4/m$) to a lower symmetry triclinic phase (space-group $I\bar{1}$) occurs. However, in $Ba_2{}^{154}SmMoO_6$ this tetragonal–triclinic distortion occurs at around 290 K, whereas, in Ba_2NdMoO_6 it occurs at the lower temperature of 130 K. Furthermore, the evolution of Mo–O bond lengths with temperature highlights a different relationship between magnetism and orbital ordering in these two materials. At 130 K a Jahn–Teller distortion was observed simultaneously with antiferromagnetic order in $Ba_2{}^{154}SmMoO_6$; the single Mo^{5+} unpaired electron occupies both the d_{xz} and d_{yz}

Department of Chemistry, University of Aberdeen, Meston Walk, Aberdeen AB24 3UE, UK. E-mail: a.c.mclaughlin@abdn.ac.uk

orbitals resulting in an elongation of the apical Mo–O bond length. In Ba_2NdMoO_6, this same JT distortion evolves over a wider temperature range 130–60 K resulting in a gradual elongation of the apical Mo–O bond well above T_N = 15 K.

Another member of this series that has generated significant interest is Ba_2YMoO_6 which is the first reported example of a valence bond glass (VBG).[19] This magnetic ground-state has been predicted theoretically,[20] and is a consequence of geometric frustration of Mo^{5+} S = 1/2 spins, which are arranged on the corners of a lattice of edge sharing tetrahedra. Consequently, all antiferromagnetic interactions cannot be satisfied simultaneously, leading to a gradual freezing of spins into a disordered pattern of spin singlets upon cooling. A subsequent study carried out on $Ba_{2-x}Sr_xYMoO_6$ showed that the VBG phase persists despite a lowering of symmetry from cubic to monoclinic ($P2_1/n$)[21] which demonstrates that the VBG phase is robust to structural distortions.

Given the remarkable behaviour seen in Ba_2YMoO_6, $Ba_2{}^{154}SmMoO_6$ and Ba_2NdMoO_6, further studies of the double perovskites Ba_2LnMoO_6 are required to build a comprehensive understanding of the magnetic and structural properties of these materials. This study focuses on the structural and magnetic properties of the molybdenum double perovskite, Ba_2GdMoO_6 which exhibits a ferroelastic phase transition below 220 K; a property that has not been reported so far for Mo^{5+} double perovskites.[13–16,18]

II. Experimental

Ba_2GdMoO_6 was prepared by solid state reaction of stoichiometric amounts of MoO_3, $BaCO_3$ and Gd_2O_3 powder of 99% purity or higher. These oxides were mixed by thorough grinding, pelletised and then heated to 800 °C and held for 15 minutes. The temperature was then raised to 1000 °C and held for 15 minutes and then finally to 1200 °C and held for 12 hours. Three further heat treatments at 1200 °C were then carried out with intermediate grinding and pelleting to ensure complete reaction and sample homogeneity. To prevent oxidation of Mo^{5+}, all heat treatments were carried out under flowing 5% H_2/N_2.

Variable temperature synchrotron X-ray diffraction patterns were recorded at a wavelength of λ = 0.3948 Å on the ID31 powder diffraction beamline at ESRF, Grenoble, France. A sample of Ba_2GdMoO_6 was inserted into a 0.5 mm-diameter borosilicate glass capillary mounted on the axis of the diffractometer and spun at ~1 Hz to improve the powder averaging of the crystallites. Diffraction patterns were recorded over a range of temperatures from 5 K to 290 K over the angular range $5^\circ < 2\theta < 45^\circ$ and rebinned to a constant step size of 0.002° for each scan.

III. Results/discussion

The variable temperature synchrotron X-ray diffraction data for Ba_2GdMoO_6 were fitted using the Rietveld refinement technique[22] using the Topas software.[23] Fig. 1 shows Rietveld refinements of

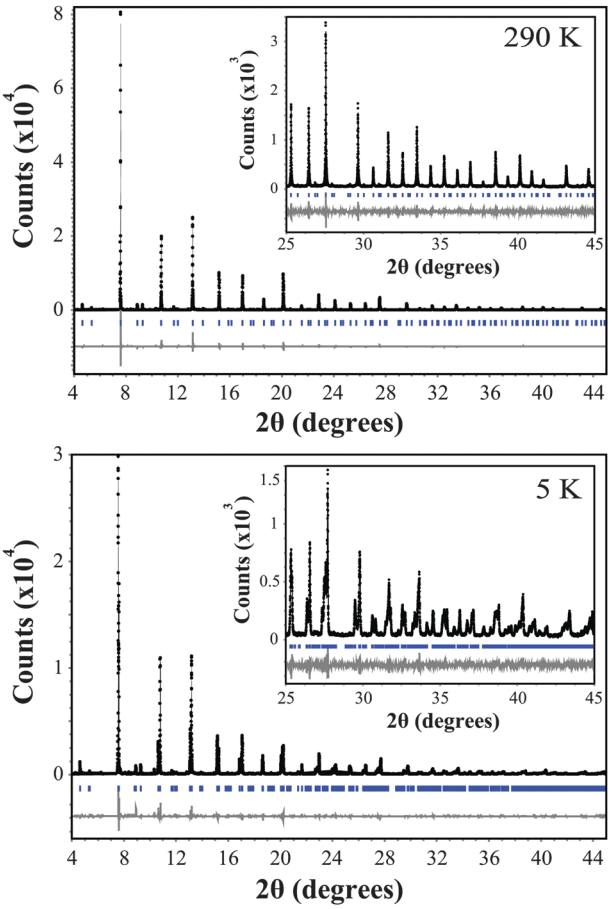

Fig. 1 Rietveld refinement of the synchrotron X-ray diffraction data for Ba_2GdMoO_6. The black line represents the actual data, the black circles represent the calculated pattern and the trace below is the difference between calculated and collected data. A region between 6.65 and 7.45 2θ (degrees) is excluded due to a peak associated with a small amount of unknown impurity.

synchrotron XRD data at both 290 K and 5 K. At 290 K, a good fit to the data was achieved with the cubic symmetry space group $Fm\bar{3}m$ [a = 8.45509(20) Å]. Upon reducing the temperature, the material undergoes a structural phase transition to the tetragonal space group $I4/m$ [a = 5.97444(20) Å, c = 8.45848(9) Å] at 220 K. This phase transition is confirmed by the observation of peak splitting below 250 K. Fig. 2 shows a selected area of the synchrotron X-ray diffraction pattern evidencing the (400) reflection at 250 K. There is clear evidence of peaks splitting below 220 K with further splitting seen in 180 K data. This transition is driven by the rotations of octahedra about the cubic (001) axis, which can be described using the Glazer tilt system ($a^0a^0c^-$). A second transition from the tetragonal space group $I4/m$ to the triclinic crystal system space group $I\bar{1}$ [($a^-a^-c^-$) Glazer tilt system, a = 5.97444(20) Å, b = 5.96863(18) Å, c = 8.45848(9) Å] occurs at 80 K, which was confirmed by the observation of further peak splitting and broadening and is corroborated by the differences in the fit statistics between the two models; χ^2 = 2.62 and 2.98 and R_{wp} = 14.96 and 17.03 for the triclinic and tetragonal models respectively at 80 K. The same phase transitions are observed for Ba_2NdMoO_6 and Ba_2SmMoO_6[13,15] upon cooling and are in

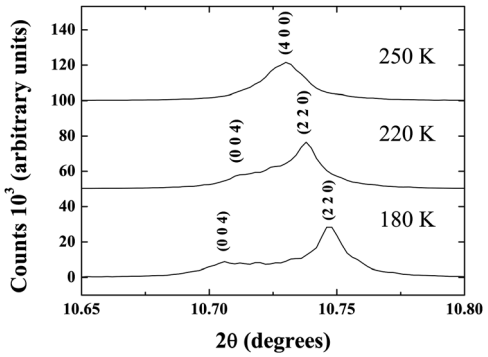

Fig. 2 A selected area of the synchrotron X-ray diffraction pattern of Ba_2GdMoO_6 showing the [400] structural peak at 250 K (top). There is clear evidence of peak splitting at the cubic to tetragonal phase transition displayed here for T = 220 K (middle) and 180 K (bottom). This peak splitting increases upon reducing the temperature.

corroboration with a recent group theoretical analysis of structural distortions of double perovskites.[7]

Upon decreasing the temperature below 220 K the quality of fit to both the tetragonal (100–220 K) and triclinic phases (5–80 K) gets progressively worse with decreasing temperature. There is clear evidence of diffuse scattering between the diffraction peaks below 220 K as shown in Fig. 3(a) which displays a close up of the [004] and [220] reflections (angular range $10.5 < 2\theta < 11$) at 5 K. The black line represents the actual data whilst the shaded region represents the calculated pattern. Such additional scattering between diffraction peaks is characteristic of a ferroelastic transition. A ferroelastic material exhibits spontaneous strain under an external stress and the transition (T_c) from the paraelastic high temperature phase to the ferroelastic low temperature phase is inherently linked to a change in symmetry of the crystal structure.[24] For Ba_2GdMoO_6 the ferroelastic transition is observed at 220 K when the crystal structure distorts from cubic to tetragonal symmetry. The spontaneous strain in a ferroelastic material is strongly influenced by the microstructure of the crystal and domains/twins are commonly observed below T_c. Scattering associated with the domain boundaries results in asymmetry in the direction of the hypothetical high symmetry peak and a characteristic *hkl*-dependent line broadening in X-ray and neutron diffraction patterns (as observed in the synchrotron X-ray diffraction data of Ba_2GdMoO_6 below 220 K). This characteristic scattering presents a challenge when attempting to extract crystallographic information from Rietveld refinement, and a range of approaches have previously been adopted.[25] Most commonly an extra phase is introduced to account for the domain wall scattering.

Fig. 3(a) shows the Rietveld refinement of the 5 K synchrotron X-ray diffraction data, modelled with the $I\bar{1}$ triclinic space group. It is clear that the model is not suitable because of the relative intensity mismatch and the unsuccessful modelling of the intensity between the peaks. The poor quality of fit is further illustrated by the goodness of fit statistics; χ^2 = 3.664, R_{wp} = 21.910 and R_p = 17.582. In order to obtain reliable

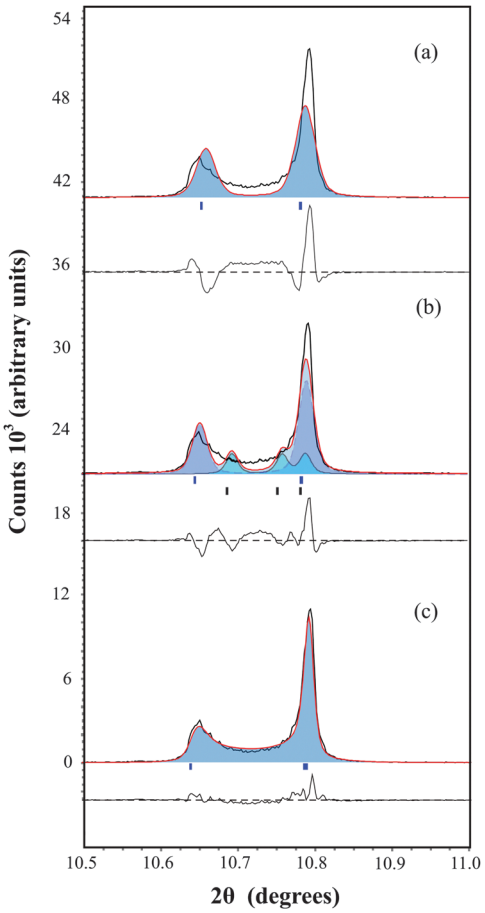

Fig. 3 Magnification of the [004] and [220] reflections at 5 K, different refinement techniques used are shown by shaded regions and correspond to: (a) conventional refinement using a single triclinic phase (b) refinement using two distinct triclinic phases attempting to model 'bulk' phase reflections and diffuse scattering separately (c) single phase model combined with anisotropic peak asymmetry, considering contributions from 'bulk' and diffuse scattering together.

crystallographic information from the Rietveld refinement an appropriate model capable of accounting for the intensity between peaks was sought. Fig. 3(a–c) shows a close up of the [004] and [220] reflections at 5 K, modelled in three different ways. Fig. 3(b) shows the two-phase model where a second crystallographically distinct phase (space group $I\bar{1}$) is incorporated into the refinement (cell parameters: a = 5.9541(2) Å, b = 5.9452(2) Å, c = 8.4778(2) Å, α = 89.971(3)°, β = 90.194(3)°, γ = 90.150(3)°) to account for the diffuse scattering originating from the domain boundaries. The refinement statistics [χ^2 = 2.866, R_{wp} = 17.139 and R_p = 13.027] show the two-phase model generates an improved fit to the 5 K data. However the introduction of a secondary phase does not fully model the intensity between peaks and only results in a minimal improvement to the fitting of the reflections associated with the primary phase.

The next approach introduced a single triclinic phase (space group $I\bar{1}$) to the refinements that incorporated anisotropic peak asymmetry. This was key as the integrated intensity is central to attaining useful structural information. Due to the

microstrained domain boundary origin of the asymmetric reflection tails, there is a well defined *hkl* dependence to the magnitude and direction of asymmetry for each peak so that an additional convolution to the peak profile was needed to adequately model the data. Two different fourth-order spherical harmonic functions were introduced in TOPAS[23] to account for both the two-theta and systematic *hkl*-dependence of the asymmetry. This fitting procedure resulted in extremely good fits across the entire dataset and could be applied successfully at all temperatures. Fig. 3(c) shows the [004] and [220] reflections at 5 K are modelled successfully by this approach. The statistical values of fit quality [χ^2 = 2.535, R_{wp} = 15.060 and R_p = 10.484] reflect the improvement in fit compared to the previous models. Crystallographic information was taken from the refined data using this approach, in the temperature range 5–290 K. The peak shapes were modelled with a pseudo-Voigt function incorporating the asymmetry described above. Refined atomic coordinates, isotropic/anisotropic thermal parameters, cell parameters, statistical measures of fit quality and selected bond lengths and angles are shown in Tables 1 and 2. All of the metal and oxygen occupancies refined to within ±1% of full occupancy and were fixed to 1. There was no evidence for cation anti-site disorder or oxygen non-stoichiometry.

Table 1 Refined atomic parameters for Ba_2GdMoO_6 including coordinates (*x*, *y*, *z*), thermal parameters, U_{iso}, cell parameters and statistical measures of fit quality at selected temperatures of variable temperature synchrotron diffraction study. Atom positions in cubic $Fm\bar{3}m$ space group at 290 K are Ba (1/4, 1/4, 1/4), Mo (0, 0, 1/2), Gd (0, 0, 0), O (0, 0, *x*). Atom positions in tetragonal *I*4/*m* space group at 220 K are Ba (0, 1/2, 1/4), Mo (1/2, 1/2, 1/2), Gd (0, 0, 0), O1 (0, 0, *z*), O2 (*x*, *y*, 0). Atom positions in triclinic $I\bar{1}$ space group at 80 K are Ba (*x*, *y*, *z*) Mo (0, 0, 1/2), Gd (0, 0, 0), O1 (*x*, *y*, *z*), O2 (*x*, *y*, *z*), O3 (*x*, *y*, *z*)

		Temperature (K)										
Atom		5	30	50	80	100	120	150	180	220	250	290
Ba	*x*	−0.0010(8)	−0.0010(8)	0.0002(8)	−0.0010(9)	0	0	0	0	0	1/4	1/4
	y	0.4997(6)	0.4999(6)	0.4998(6)	0.5000(9)	1/2	1/2	1/2	1/2	1/2	1/4	1/4
	z	0.2507(4)	0.2508(4)	0.2507(4)	0.2497(5)	1/4	1/4	1/4	1/4	1/4	1/4	1/4
	U_{iso} (Å^2)	0.00253(5)	0.00233(5)	0.00253(5)	0.00299(5)	0.00305(5)	0.00331(5)	0.00385(5)	0.00440(5)	0.00520(5)	0.00714(5)	0.00811(5)
Gd	U_{iso} (Å^2)	0.00253(5)	0.00233(5)	0.00253(5)	0.00299(5)	0.00305(5)	0.00331(5)	0.00385(5)	0.00440(5)	0.00520(5)	0.00714(5)	0.00811(5)
Mo	U_{iso} (Å^2)	0.00253(5)	0.00233(5)	0.00253(5)	0.00299(5)	0.00305(5)	0.00331(5)	0.00385(5)	0.00440(5)	0.00520(5)	0.00714(5)	0.00811(5)
O1	*x*	−0.003(7)	−0.003(7)	−0.002(7)	0.004(7)	0	0	0	0	0	0.2709(4)	0.2710(4)
	y	0.008(4)	0.008(4)	0.008(4)	0.017(3)	0	0	0	0	0	0	0
	z	0.2662(10)	0.2670(10)	0.2671(9)	0.2661(10)	0.2724(11)	0.2723(11)	0.2724(13)	0.2723(16)	0.2714(23)	0	0
	U_{iso} (Å^2)	0.0073(13)	0.0070(13)	0.0071(13)	0.0081(13)	0.0113(12)	0.0103(11)	0.0139(12)	0.0157(10)	0.0157(12)	0.0132(1)	0.0133(1)
O2	*x*	0.238(3)	0.236(3)	0.239(3)	0.271(3)	0.290(2)	0.289(2)	0.286(2)	0.275(4)	0.268(5)	—	—
	y	0.317(3)	0.315(3)	0.316(3)	0.255(4)	0.253(2)	0.254(2)	0.258(2)	0.268(5)	0.277(5)	—	—
	z	0.003(3)	0.002(3)	0.004(3)	0.001(4)	0	0	0	0	0	—	—
	U_{iso} (Å^2)	0.0073(13)	0.0070(13)	0.0071(13)	0.0081(13)	0.0113(12)	0.0103(11)	0.0139(12)	0.0157(10)	0.0157(12)	—	—
O3	*x*	0.724(3)	0.722(3)	0.725(3)	0.744(3)	—	—	—	—	—	—	—
	y	0.262(4)	0.263(4)	0.264(4)	0.317(3)	—	—	—	—	—	—	—
	z	−0.005(4)	−0.004(4)	−0.005(4)	−0.007(3)	—	—	—	—	—	—	—
	U_{iso} (Å^2)	0.0073(13)	0.0070(13)	0.0071(13)	0.0081(13)	—	—	—	—	—	—	—
	a (Å)	5.93893(8)	5.93934(8)	5.94043(8)	5.94639(10)	5.95213(4)	5.95612(3)	5.96055(3)	5.96470(4)	5.96990(4)	8.45150(2)	8.45509(2)
	b (Å)	5.93990(9)	5.94046(10)	5.94190(9)	5.94701(11)	—	—	—	—	—	—	—
	c (Å)	8.51813(9)	8.51758(9)	8.51483(9)	8.50201(11)	8.49183(7)	8.48442(6)	8.47788(6)	8.47159(7)	8.46457(9)	—	—
	α (°)	89.8673(12)	89.8677(11)	89.8660(11)	89.8614(11)	90.0	90.0	90.0	90.0	90.0	90.0	90.0
	β (°)	89.9493(12)	89.9495(12)	89.9511(12)	89.9587(13)	90.0	90.0	90.0	90.0	90.0	90.0	90.0
	γ (°)	89.9830(13)	89.9850(13)	89.9833(13)	89.9793(17)	90.0	90.0	90.0	90.0	90.0	90.0	90.0
	χ^2	2.530	2.528	2.627	2.614	2.635	2.510	2.463	2.432	2.505	2.344	2.290
	R_{wp} (%)	15.026	15.352	14.881	14.948	15.271	14.708	14.609	14.536	15.075	14.275	14.046
	R_p (%)	10.448	10.680	10.084	9.943	10.875	10.015	9.871	9.682	10.160	10.990	11.095

Table 2 Refined Mo–O, Gd–O and Ba–O bond lengths along with Mo–O–Gd bond angles for Ba_2GdMoO_6, as a function of temperature. At 220 K the crystal symmetry changes from cubic (space group $Fm\bar{3}m$) to tetragonal (space group *I*4/*m*), with a further structural phase transition to triclinic (space group $I\bar{1}$) at 80 K

	Temperature (K)										
Bond	5	30	50	80	100	120	150	180	220	250	290
Mo–O(1) (Å)	1.990(8)	1.988(8)	1.983(8)	1.979(9)	1.93(1)	1.932(9)	1.930(11)	1.929(13)	1.935(20)	1.936(3)	1.936(3)
Mo–O(2) (Å)	1.897(16)	1.912(16)	1.896(15)	1.898(18)	1.931(9)	1.930(9)	1.927(12)	1.929(26)	1.923(32)	—	—
Mo–O(3) (Å)	1.942(21)	1.928(21)	1.940(21)	1.94(3)	—	—	—	—	—	—	—
Gd–O(1) (Å)	2.270(8)	2.272(8)	2.276(8)	2.274(9)	2.31(1)	2.310(9)	2.309(11)	2.307(13)	2.298(20)	2.290(3)	2.291(3)
Gd–O(2) (Å)	2.260(21)	2.274(20)	2.263(21)	2.267(26)	2.290(9)	2.293(9)	2.295(12)	2.289(26)	2.299(32)	—	—
Gd–O(3) (Å)	2.356(16)	2.341(16)	2.356(15)	2.340(19)	—	—	—	—	—	—	—
Mo–O(1)–Gd (°)	177.2(14)	177.3(14)	177.3(14)	177.2(16)	180.0	180.0	180.0	180.0	180.0	180.0	180.0
Mo–O(2)–Gd (°)	176.1(15)	176.0(14)	176.4(15)	177.5(17)	171.5(5)	172.9(5)	173.4(6)	178.3(14)	177.8(17)	—	—
Mo–O(3)–Gd (°)	161.8(9)	161.9(9)	162.2(8)	165.6(10)	—	—	—	—	—	—	—

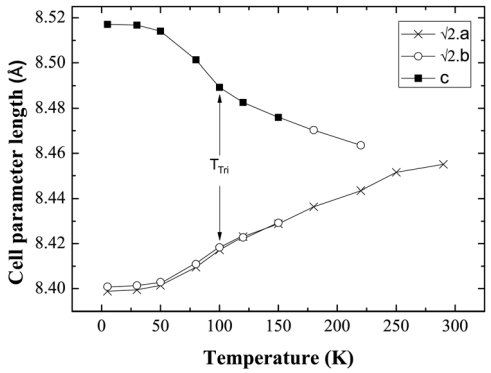

Fig. 4 Evolution of the cell parameters with temperature evidencing a structural transition to triclinic symmetry below 100 K (T_{Tri}); *a* and *b* have been multiplied by $\sqrt{2}$ for ease of comparison.

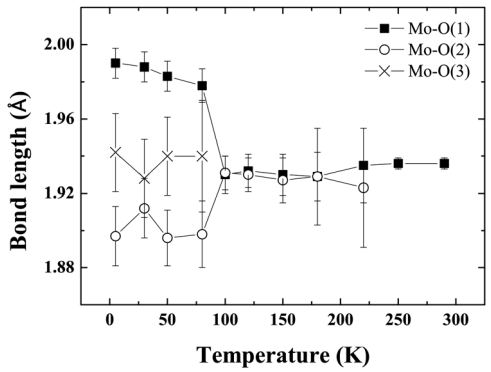

Fig. 5 The thermal evolution of the Mo–O bond lengths in Ba_2GdMoO_6. There is no evidence of the Jahn–Teller distortion previously reported for Ba_2LnMoO_6 (Ln = Nd, Sm).

Fig. 4 shows the evolution of cell parameters in the temperature range 5–290 K. The tetragonal to triclinic transition is manifest in the cell parameters where a slight elongation along *c*, coinciding with a contraction along *a* is detected. Fig. 5 shows the evolution of Mo–O bond lengths with temperature down to 5 K. The triclinic structural phase transition is manifest in the Mo–O(1) and Gd–O(1) bond lengths which elongate and contract respectively below 100 K (Fig. 5, Table 2). In contrast Gd–O(2) exhibits a smooth reduction upon cooling. The Mo–O–Gd bond angles are reported in Table 2 and the tetragonal to triclinic phase transition is clearly evident in thermal variation of the Mo–O(2)–Gd bond angles where a reduction in the buckling of Mo–O(2)–Gd is observed below 100 K.

There is no evidence of the Jahn–Teller distortion previously reported for Ba_2NdMoO_6[13] and Ba_2SmMoO_6.[15] The disappearance of the Jahn–Teller distortion is probably related to the reduced distortion of the MoO_6 octahedra in Ba_2GdMoO_6. Upon replacing Nd with Gd in Ba_2LnMoO_6 the Goldschmidt tolerance factor[26] increases from 0.975 to 0.985. It is known that when $t < 1$, B–O and B′–O bonds within the structure are compressed, whilst A–O bonds are stretched[27] so that octahedral rotations and tilts occur to alleviate stress. If the tolerance factor

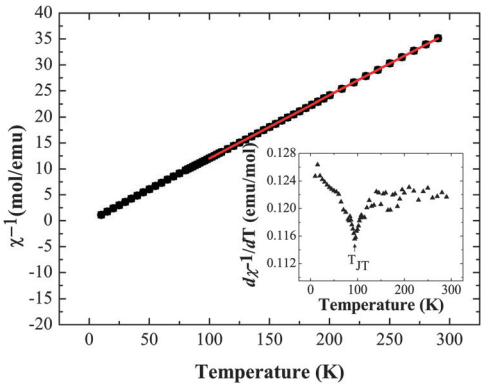

Fig. 6 Inverse magnetic susceptibility data χ^{-1} *vs. T* and $d\chi^{-1}/dT$ *vs. T* (inset) for Ba_2GdMoO_6, evidencing the structural transition from tetragonal to triclinic symmetry below 100 K.

is very close to 1, then the ideal cubic structure should be observed. The results here suggest that a minimum distortion is required in order to evidence the Jahn–Teller distortion in Mo^{5+} double perovskites; otherwise the electronic stability conferred by the Jahn–Teller is insufficient to induce a further deformation of the structure. The results also suggest that the Jahn–Teller distortion present in Ba_2LnMoO_6 (Ln = Nd, Sm) stabilises the tetragonal to triclinic transition; when the Jahn–Teller distortion is no longer apparent T_{tri} is observed at a much lower temperature (T_{tri} = 130 K, 290 K and 80 K for Ln = Nd, Sm and Gd respectively). Further variable temperature diffraction studies on other members of the Ba_2LnMoO_6 series are required in order to understand the complex coupling between structural and Jahn–Teller distortions in Mo^{5+} double perovskites.

Magnetic susceptibility measurements were also performed on Ba_2GdMoO_6; Fig. 6 shows the temperature variation of χ^{-1} and $d\chi^{-1}/dT$. There is no evidence of a magnetic transition down to 2 K. A Curie–Weiss fit to the susceptibility data between 300 K and 100 K yields a Weiss temperature of θ = 2.35 K and a Curie constant, *C* of 8.18 emu mol^{-1} K^{-1}, corresponding to an overall effective moment of 8.14 μ_B, close to the predicted total magnetic moment of 8.13 μ_B. Below 100 K, the inverse susceptibility deviates from the Curie–Weiss law. Fig. 6 (inset) evidences a subtle peak in the thermal evolution of $d\chi^{-1}/dT$ at 100 K, which correlates with the tetragonal to triclinic structural transition temperature reported above.

IV. Conclusions

The results demonstrate that the double perovskite Ba_2GdMoO_6 is ferroelastic, whereby it exhibits spontaneous strain under an external stress. Such an effect has not been reported previously for Mo^{5+} double perovskites. This ferroelastic transition is manifest in synchrotron X-ray diffraction patterns as diffuse scattering associated with scattering from domain boundaries is detected below the cubic to tetragonal phase transition at 220 K. In order to model this and gain useful

crystallographic information, the peak asymmetry was convoluted with a fourth order spherical harmonic (SH), to model the direction and magnitude of peak asymmetry. Ba_2GdMoO_6 undergoes a transition from a cubic (space group $Fm\bar{3}m$) to a tetragonal system (space group $I4/m$) at 220 K before undergoing a second transition to a triclinic system (space group $I\bar{1}$) at 80 K. Magnetic susceptibility data shows a deviation from Curie–Weiss behaviour below 100 K which coincides with the structural transition from tetragonal to cubic symmetry.

References

1 J. Fontcuberta, B. Martinez, A. Seffar, S. Piñol, J. L. García-Muñoz and X. Obradors, *Phys. Rev. Lett.*, 1996, **76**, 1122–1125.
2 G. Shirane, H. Danner and R. Pepinsky, *Phys. Rev. B: Condens. Matter Mater. Phys.*, 1957, **105**, 856–860.
3 H. Khosroabadi, J. Kobayashi, K. Tanaka, S. Miyasaka, S. Tajima, H. Uchiyama and A. Q. R. Baron, *J. Supercond. Novel Magn.*, 2010, **23**, 1385–1389.
4 N. Orlovskaya, Y. Gogotsi, M. Reece, B. Cheng and I. Ginson, *Acta Mater.*, 2002, **50**, 715–723.
5 M. T. Anderson, K. B. Greenwood, G. A. Taylor and K. R. Poeppelmeier, *Prog. Solid State Chem.*, 1993, **22**, 197–233.
6 P. M. Woodward, *Acta Crystallogr., Sect. A: Fundam. Crystallogr.*, 1997, **53**, 32–43.
7 C. J. Howard, B. J. Kennedy and P. M. Woodward, *Acta Crystallogr., Sect. B: Struct. Sci.*, 2003, **59**, 463–471.
8 J.-W. G. Bos, J. P. Attfield, T.-S. Chan, R.-S. Liu and L.-Y. Jang, *Phys. Rev. B: Condens. Matter Mater. Phys.*, 2005, **72**, 014101.
9 D. Y. Chen, F. Z. Chien, D. C. Ling, J. L. Tseng, S. R. Sheen, M. J. Wang and M. K. Wu, *Physica C*, 1997, **282–287**, 73–76.
10 C. Bernuy-Lopez, M. Allix, C. A. Bridges, J. B. Claridge and M. J. Rosseinsky, *Chem. Mater.*, 2007, **19**, 1035–1043.
11 K.-I. Kobayashi, T. Kimura, H. Sawada, K. Terakura and Y. Tokura, *Nature*, 1998, **395**, 677.
12 H. Boysen, *Z. Kristallogr.*, 2005, **220**, 726–734.
13 E. J. Cussen, D. R. Lynham and J. Rogers, *Chem. Mater.*, 2006, **18**, 2855–2866.
14 A. C. McLaughlin, *Solid State Commun.*, 2006, **137**, 354–357.
15 A. C. Mclaughlin, *Phys. Rev. B: Condens. Matter Mater. Phys.*, 2008, **78**, 132404.
16 T. K. Wallace, C. Ritter and A. C. Mclaughlin, *J. Solid State Chem.*, 2012, **196**, 379–383.
17 R. D. Shannon, *Acta Crystallogr., Sect. A: Cryst. Phys., Diffr., Theor. Gen. Cryst.*, 1976, **32**, 751–767.
18 E. J. Cussen and W. J. Cameron, *J. Mater. Chem.*, 2010, **20**, 1340–1347.
19 A. C. Mclaughlin, M. A. de Vries and J.-W. G. Bos, *Phys. Rev. Lett.*, 2010, **104**, 177202.
20 M. Tarzia and G. Biroli, *EuroPhys. Lett.*, 2008, **82**, 67008.
21 A. C. Mclaughlin, M. A. de Vries and J.-W. G. Bos, *Phys. Rev. B: Condens. Matter Mater. Phys.*, 2010, **82**, 094424.
22 H. Rietveld, *J. Appl. Crystallogr.*, 1969, **2**, 65–71.
23 TOPAS, program available from Bruker AXS GmbH, Ostliche Rheinbrukenstrasse 50, 76187 Karlsruhe, Germany.
24 E. K. H. Salje, *Phase transitions in ferroelastic and co-elastic crystals*, Cambridge University Press, Cambridge, 1991.
25 I. Grinberg, M. R. Suchomel, W. Dmowski, S. E. Mason, H. Wu, P. K. Davies and A. M. Rappe, *Phys. Rev. Lett.*, 2007, **98**, 107601.
26 V. M. Goldschmidt, *Die Naturwissenschaften*, 1926, **14**, 477–485.
27 J. B. Goodenough, *Rep. Prog. Phys.*, 2004, **67**, 1915–1993.